# Compact SIDGS Filtering Power Divider With Three-Port 10-GHz Reflectionless Range

Qingxian Li, *Student Member, IEEE*, Hongxin Tang, *Graduate Student Member, IEEE*, Deshan Tang, *Student Member, IEEE*, Zhixian Deng, *Graduate Student Member, IEEE*, and Xun Luo, *Senior Member, IEEE*

***Abstract*—In this brief, a compact high isolation filtering power divider (FPD) with wide stopband and wide-band three-port reflectionless operation is proposed. Such FPD consists of a trigonometric substrate-integrated defected ground structure (SIDGS) based resonator and three absorptive networks. The good stopband performance is achieved by using the trigonometric SIDGS. Meanwhile, the absorptive networks based on common-gate topology capable of absorbing the out-of-band reflected signals are connected to the SIDGS resonator, which provides the wideband reflectionless operation in all three ports of the FPD. To verify the mechanisms mentioned above, a FPD operated at 2.10 GHz (i.e., $f_0$) is fabricated, which exhibits a 42 dB stopband rejection level up to 20 GHz (i.e., $9.5f_0$). The measured reflectionless range with return loss lower than −10 dB is up to 10 GHz in all three ports. The core size of the FPD is about 0.36 $\lambda_g$ × 0.38 $\lambda_g$, where $\lambda_g$ is the microstrip guided wavelength at the center frequency.**

***Index Terms*—Filtering power divider, high isolation, reflectionless, substrate-integrated defected ground structure (SIDGS), wide stopband.**

## I. Introduction

As ONE of key components in practical wireless systems, power divider with high performance is dramatically demanded. To reduce the out-of-band interferences, the filtering power dividers (FPDs) with high isolation and wide stopband are presented [1]–[7]. However, those power dividers reflect the out-of-band signal back to the source. Such reflected signal may cause the intermodulation interference and gain fluctuations once the power divider is connected to the nonlinear devices, e.g., mixer and high gain amplifier. Recent researches show that the system performance degeneration caused by the out-of-band reflection signals can be eliminated by using the reflectionless components [8]–[10]. The reflected signal is absorbed by the reflectionless components. Conventional reflectionless components using a symmetrical networks with complementary even- and odd-mode equivalent circuits [11]–[14] to achieve a two-port reflectionless operation. However, the passband performance of such reflectionless components is relatively poor due to the requirement of multiple lossy lumped components. By introducing an auxiliary signal path to absorb the out-of-band reflection signal, a wideband reflectionless operation can be obtained without sacrificing the passband performance [15]–[21]. Nonetheless, such topology suffers from the relatively larger circuit size, especially for the multi-port reflectionless components. Therefore, the design of compact FPD with three-port reflectionless operation still remains great challenge.

In this brief, a compact FPD is proposed, which can achieve wide reflectionless range in three ports. A trigonometric substrate-integrated defected ground structure (SIDGS) with T-stub feed-line is introduced for the filtering function of the power divider. The absorptive networks based on common-gate (CG) topology are cascaded in the input and output ports to achieve the three-port reflectionless operation. Based on the structures mentioned above, a reflectionless FPD is designed and fabricated. A good agreement between measurement and simulation is achieved.

Manuscript received January 4, 2022; revised March 15, 2022; accepted April 1, 2022. Date of publication April 8, 2022; date of current version June 29, 2022. This work was supported in part by the National Natural Science Foundation of China under Grant 62161160310 and Grant 61934001. This brief was recommended by Associate Editor L. B. Oliveira. *(Corresponding author: Xun Luo.)*

The authors are with the Center for Advanced Semiconductor and Integrated Micro-System, University of Electronic Science and Technology of China, Chengdu 611731, China (e-mail: xun-luo@ieee.org).

Color versions of one or more figures in this article are available at https://doi.org/10.1109/TCSII.2022.3165848.

Digital Object Identifier 10.1109/TCSII.2022.3165848

## II. Schematic and Operation

Fig. 1 shows the configuration of the proposed FPD, which consists of trigonometric SIDGS cells and three absorptive networks. The SIDGS resonator located on the Ground I layer is fed by three T-stub at the top layer. Meanwhile, a resistor at the top layer is connected between the microstrip feed-line of port 2 and port 3. Besides, the absorptive networks are cascaded with the microstrip feed-lines of the SIDGS resonator. To investigate the mechanisms of the proposed structure, the RO4003 substrate (i.e., $\varepsilon_r = 3.55$, $h_1 = 0.203$ mm and $h_2 = 0.303$ mm), EM simulator IE3D, and design tool ADS are used.

### A. Power Divider With Trigonometric SIDGS Cell

The configuration of the proposed SIDGS resonator cells are shown in Fig. 2(a) and (c). Such SIDGS cell is composed of two ground planes connected by surrounding metal-vias [22]–[23]. As discussed in [5], the SIDGS resonator is similar to a λ/2 SIR with two ground ends. The fundamental resonant frequency can be calculated by equation (1)–(3), shown at the bottom of the next page. The resonant frequency of the proposed SIDGS cell 1 is varied with $s_3$ and $d_4$, while the resonances of cell 2 and cell 3 are adjusted by $s_4$ and $d_5$. Fig. 2(b) and (d) reveals that the calculation shows good agreement with simulation. To verify the harmonic characteristic of the SIDGS cell 1, the simulated transmission responses in the weak-coupled feeding scheme is presented in Fig. 3. Note

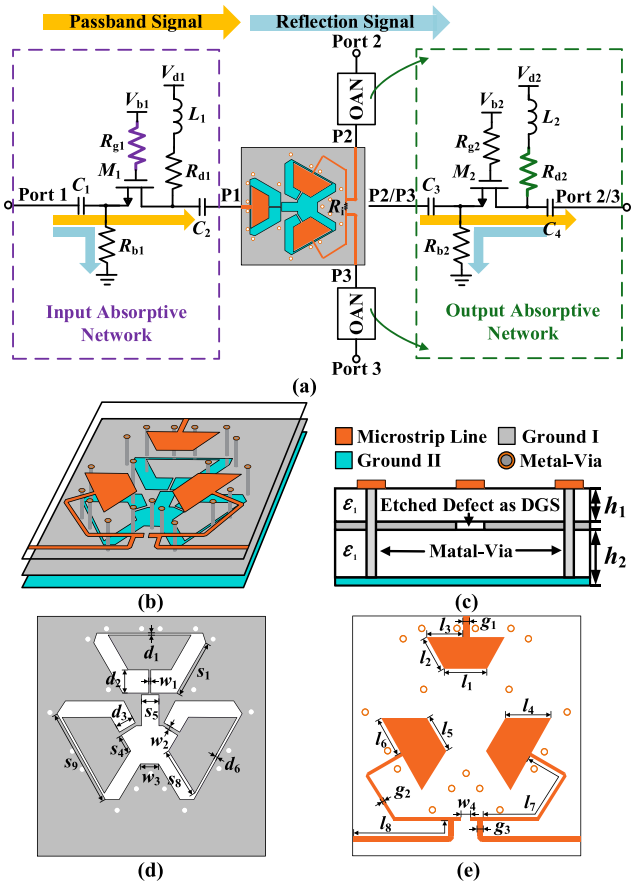


Fig. 1. (a) Schematic of the proposed three-port reflectionless FPD. (b) 3D view of the layout. (c) Layer diagram. (d) Details of the middle layer. (e) Details of the top layer.

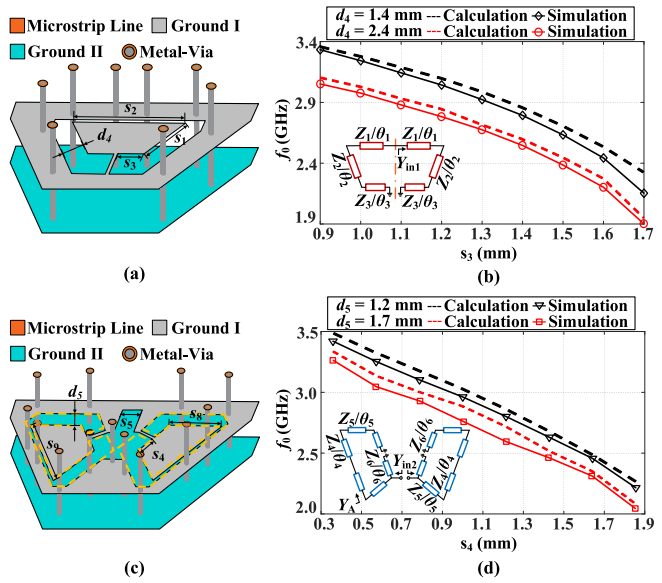


Fig. 2. Configuration of the proposed SIDGS resonant cell. (a) 3-D view of cell 1. (b) Simplified equivalent circuit model and comparison of calculated and simulated fundamental resonance of cell 1. (c) 3-D view of cell 2 and cell 3. (d) Simplified equivalent circuit model and comparison of calculated and simulated fundamental resonance of cell 2 and cell 3.

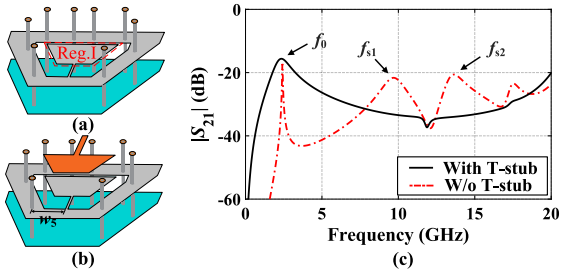


Fig. 3. (a) The resonant cell without T-stub. (b) The resonant cell with T-stub. (c) Simulated frequency responses of the SIDGS resonant cell in different configurations.

that the harmonic of the SIDGS cell 1 is mainly caused by the TEM spurious resonant mode due to the rectangular metal patch in Reg. I. To suppress the harmonic, a strong-coupled T-stub is located symmetrically over the cell [5]. As shown in Fig. 4(c), compare to the weak-coupled feeding scheme, the harmonic can be suppressed by strong-coupled T-stub. The harmonic characteristic of cell 2 and cell 3 is similar to cell 1. Thus, the T-stub can also be used to suppress the harmonics. Besides, a transmission zero (TZ) is created by the short-circuited λ/4 lines embedded in the SIDGS structure. Such TZ can be controlled by adjusting the distance from the metal-vias to resonator (i.e., $w_5$) [24]. To achieve the filtering power division, three coupled SIDGS resonant cells are utilized, as exhibited in Fig. 4(a). The cell 1 is the input cell, while the cell 2 and 3 are configured into a symmetrical structure to form the output cells. The 2-port second-order topology are used for simplifying the analysis of the symmetrical 3-port circuit, where $k_{12}$ is equal to $k'_{12}/\sqrt{2}$ to achieve the same source impedance in two circuits [25]. Then, the coupling matrix $[M_p]$ to meet the design specifications (i.e., center at 2.10 GHz with 3-dB bandwidth of 24%) is expressed as:

$$[M_p] = \begin{bmatrix} 0 & 0.85 & 0 & 0 \\ 0.85 & -0.06 & 0.72 & 0 \\ 0 & 0.72 & -0.02 & 0.85 \\ 0 & 0 & 0.85 & 0 \end{bmatrix} \tag{4}$$

The theoretical $S$-parameters calculated by coupling matrix exhibits a good agreement with the EM-simulation, as shown in Fig. 4(b). Fig. 5(a) exhibits that the coupling coefficient $k_{12}$ is adjusted by the dimension $w_5$ and $s_6$. Meanwhile, an additional etched defect is placed between cell 2 and cell 3 to decrease the coupling between R2 and R3. Fig. 5(b) shows that the coupling coefficient $k_{23}$ is tiny with suitable $s_5$ and $s_7$. Besides, Fig. 5(c) exhibits that the external quality $Q_e$ is effected by the size of T-stub. Then, a resistor is introduced to achieve good isolation between port 2 and port 3. Here, the

$$Y_{in1} = -j\frac{1}{Z_1}\frac{Z_1Z_2 - Z_1Z_3\tan\theta_2\tan\theta_3 - Z_2Z_3\tan\theta_1\tan\theta_3 - Z_2^2\tan\theta_1\tan\theta_3}{Z_2Z_3\tan\theta_3 + Z_2^2\tan\theta_2 + Z_1Z_2\tan\theta_1 - Z_1Z_3\tan\theta_1\tan\theta_2\tan\theta_3} \tag{1}$$

$$Y_{in2} = \frac{1}{jZ_6\tan\theta_6} + \frac{Z_5 + j\tan\theta_5/Y_A}{Z_5(1/Y_A + jZ_5\tan\theta_5)} \tag{2}$$

$$Y_A = -j\frac{1}{Z_5}\frac{Z_5Z_4 - Z_5Z_6\tan\theta_4\tan\theta_6 - Z_4Z_6\tan\theta_5\tan\theta_6 - Z_4^2\tan\theta_5\tan\theta_6}{Z_4Z_6\tan\theta_6 + Z_4^2\tan\theta_4 + Z_5Z_4\tan\theta_{21} - Z_5Z_6\tan\theta_5\tan\theta_4\tan\theta_6} \tag{3}$$

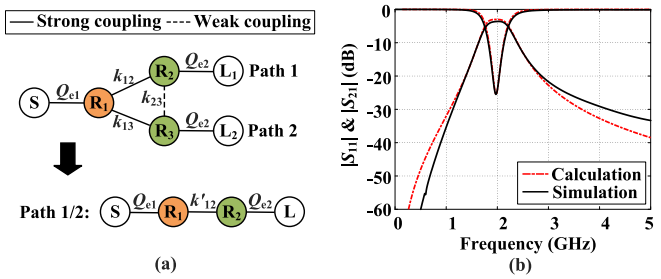


Fig. 4. (a) Coupling topologies of the proposed FPD and simplified 2-port circuit. (b) Simulated and calculated $|S_{11}|$ and $|S_{21}|$ of the FPD.

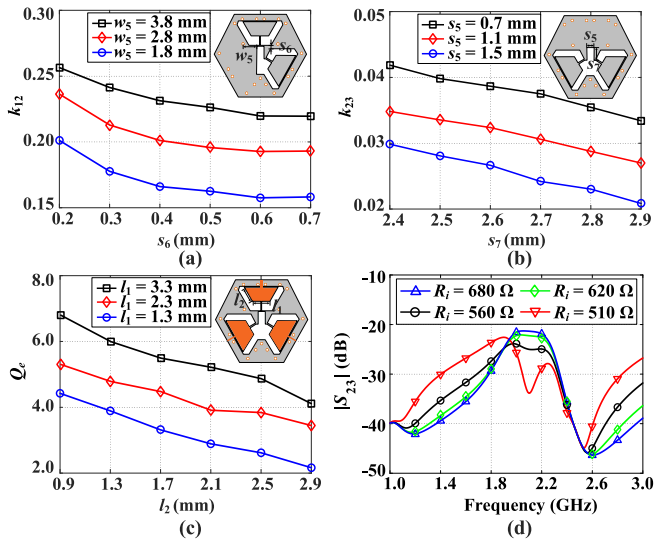


Fig. 5. (a) Effects of dimension $w_5$ and $S_6$ on the coupling coefficient $k_{12}$. (b) Efforts of dimension $S_5$ and $S_7$ on the coupling coefficient $k_{23}$. (c) Effects of dimension $l_1$ and $l_2$ on the external $Q_e$. (d) Effects of the resistor $R_i$ on the isolation.

isolation resistor is directly loaded on the feed-line of cell 2 and cell 3. As shown in Fig. 5(d), the optimized resistance $R_i$ of 560 Ω is used to achieve improved isolation.

### *B. Input and Output Absorptive Networks*

The reflectionless operation in the input- and output-ports are provided by the absorptive networks. Such absorptive networks are implemented based on CG topology in this brief, as shown in Fig. 6(a). The small signal equivalent circuit of the proposed absorptive network is exhibited in Fig. 6(b). The input and output impedance (i.e., $Z_{in}$ and $Z_{out}$, respectively) can be calculated by equation (5)–(6), shown at the bottom of the page, where the parameters $Z_{gd}$, $Z_{gs}$, $Z_{ds}$, $Z_d$, and $K$ are expressed as:

$$Z_{gd} = R_g + 1/sC_{gd} \tag{7}$$

$$Z_{gs} = R_g + 1/sC_{gs} \tag{8}$$

$$Z_{ds} = r_{ds}||1/sC_{ds} \tag{9}$$

$$Z_d = R_d + sL \tag{10}$$

$$K = \frac{1/Z_{ds} - 1/R_b - 1/Z_{gs}}{(g_m + g_{mb})(1 - R_g/Z_{gs}) + 1/Z_{ds}} \tag{11}$$

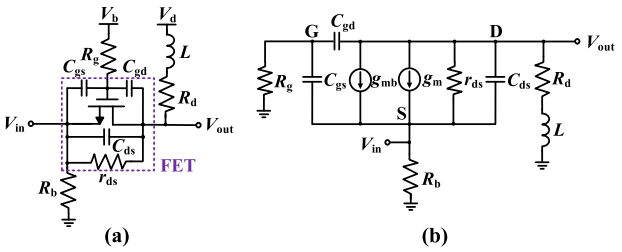


Fig. 6. (a) Schematic of the proposed absorptive network based on CG topology. (b) Small signal equivalent circuit of proposed absorptive network.

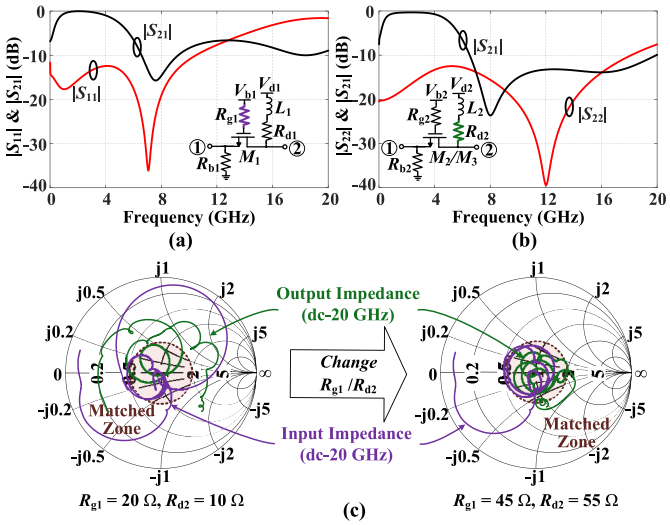


Fig. 7. (a) Simulated $|S_{11}|$ and $|S_{21}|$ of the input absorptive network. (b) Simulated $|S_{22}|$ and $|S_{21}|$ of the output absorptive network. (c) Calculated input and output impedance of the FPD with different $R_{g1}$ and $R_{d2}$ from dc to 20 GHz.

Here, the $g_m$ and $g_{mb}$ are the transconductance of the transistor FET, while the $r_{ds}$, $C_{gs}$, $C_{ds}$, and $C_{gd}$ are the parasitic resistor and capacitors of the transistor FET, respectively. The complete reflectionless FPD has been exhibited in Fig. 1(a), two identical output absorptive networks are loaded to the P2 and P3, while the input absorptive network is connected to the P1. As shown in Fig. 7(a) and (b), good reflectionless performance can be achieved at the three ports of FPD by using the proposed input- and output-absorptive networks. The reflectionless operation at port 1 is achieved by the intrinsic wideband impedance matching of CG topology, while the out-of-band reflection signals are mainly absorbed by the resistor $R_{g1}$. Meanwhile, the output impedance of the absorptive network can be adjusted by the $R_{d2}$ and $L_2$ to achieve wideband reflectionless operation. To achieve a good reflectionless operation without affecting the passband performance, the absorptive networks should match to the SIDGS resonator in the passband and provide a wideband impedance matching at the input- and output-ports of the FPD. Here, the inductors $L_1$, $L_2$ and capacitors $C_2$, $C_3$ are optimized to achieve a good in-band impedance matching with the SIDGS resonator.

$$Z_{in} = \frac{Z_{ds} + Z_d}{[(g_m + g_{mb})(R_g/Z_{gs} - 1) - 1/R_b - 1/Z_{gs}]Z_{ds} - (1/R_b + 1/Z_{gs})Z_d + 1} \tag{5}$$

$$Z_{out} = \frac{1}{(1 - K)/Z_{ds} + K(g_m + g_{mb})(R_g/Z_{gs} - 1) + 1/Z_d + 1/Z_{gd}} \tag{6}$$

TABLE I
COMPARISON OF STATE-OF-THE-ART FPD

| Ref. | [4] | [5] | [20] | [26] | [27] | [28] | **This work** |
|---|---|---|---|---|---|---|---|
| Tech.* | DGS | SIDGS | Microstrip | Microstrip | Microstrip | Microstrip | **SIDGS** |
| $f_0$ # (GHz) | 2.31 | 2.87 | 1.04–1.38 | 1.0 | 2.04 | 2.0 | **2.10** |
| IL** (dB) | 1.2 | 1.0 | N/A | 1.3 | 0.9 | 2.1 | **1.2** |
| Reflectionless Operation | N/A | N/A | 1 port | 2 ports | 3 ports | 3 ports | **3 ports** |
| BW of $\|S_{11}\| < -10$ dB | N/A | N/A | 0.76–1.79 GHz | N/A | 1.1–2.9 GHz$^{\diamond}$ | 1.3–2.7 GHz$^{\diamond}$ | **dc–10 GHz** |
| BW of $\|S_{22}\|$ and $\|S_{33}\| < -10$ dB | N/A | N/A | N/A | 0.5–1.5 GHz$^{\diamond}$ | 1.3–2.7 GHz$^{\diamond}$ | 1.3–2.7 GHz$^{\diamond}$ | **dc–13 GHz** |
| Stopband Rejection | >30 dB up to 20 GHz | >28 dB up to 20 GHz | N/A | N/A | N/A | N/A | **>42 dB up to 20 GHz** |
| Passband Isolation | >17 dB | >20 dB | >10 dB | >20 dB | >12.9 dB | >43 dB | **>20 dB** |
| Core Circuit Size | 0.38 $\lambda_g^2$ | 0.10 $\lambda_g^{2\diamond\diamond}$ | 0.09 $\lambda_g^2$ | N/A | N/A | 3.41 $\lambda_g^2$ | **0.14 $\lambda_g^{2\diamond\diamond}$** |

*: Technology used for power divider design. #: Center frequency.
**: Passband insertion loss. $^{\diamond}$: Estimated from figures. $^{\diamond\diamond}$: Three metal layers.

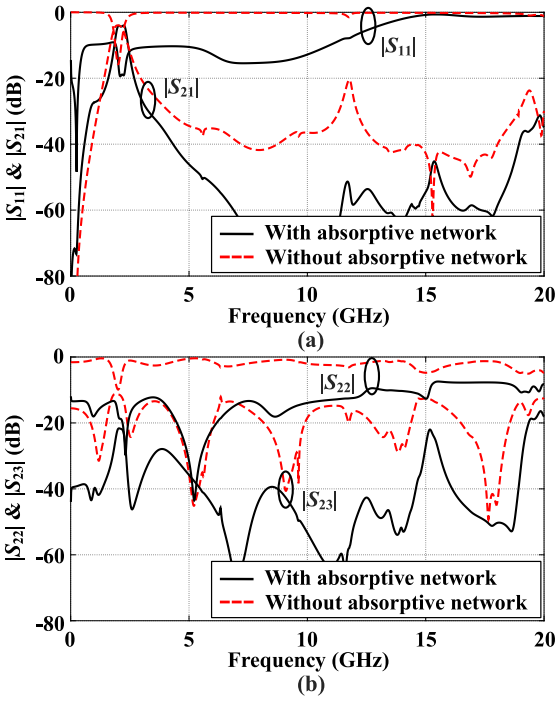


Fig. 8. Effects of the absorptive networks on the frequency responses of the proposed FPD. (a) $|S_{11}|$ and $|S_{21}|$. (b) $|S_{22}|$, $|S_{33}|$ and $|S_{23}|$.

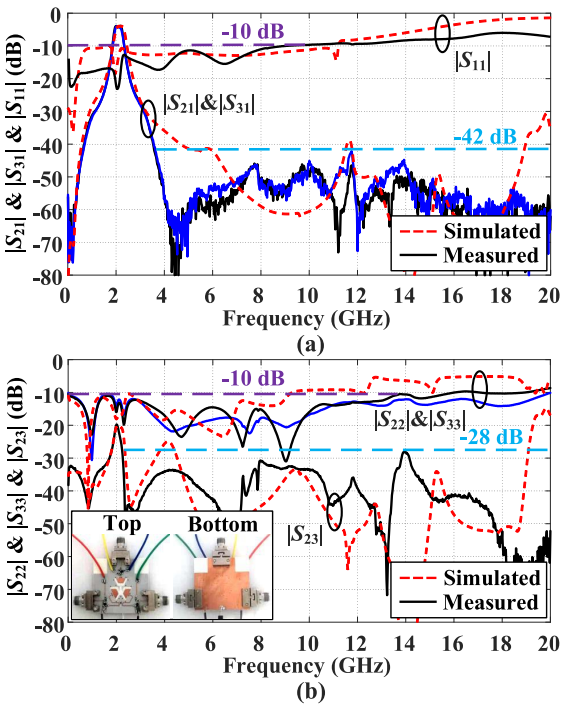


Fig. 9. Measured and simulated $S$-parameters of the proposed FPD prototype. ($l_1 = 3.3$, $l_2 = 3.4$, $l_3 = 3.2$, $l_4 = 3.9$, $l_5 = 3.3$, $l_6 = 3.4$, $l_7 = 13.1$, $l_8 = 9.1$, $s_1 = 4.8$, $s_2 = 7.0$, $s_3 = 1.7$, $s_4 = 1.5$, $s_5 = 1.5$, $s_6 = 0.7$, $s_7 = 2.8$, $s_8 = 4.1$, $s_9 = 8.3$, $w_1 = 0.1$, $w_2 = 0.2$, $w_3 = 1.7$, $w_4 = 0.4$, $w_5 = 2.8$, $d_1 = 0.1$, $d_2 = 1.9$, $d_3 = 1.7$, $d_4 = 1.3$, $d_5 = 1.4$, $g_1 = 0.4$, $g_2 = 0.3$, and $g_3 = 0.4$, unit: mm. $L_1 = 43$ nH, $L_2 = 1.3$ nH, $C_1 = 1$ nF, $C_2 = 100$ pF, $C_3 = 33$ pF, $C_4 = 1$ nF, $R_{g1} = 43\ \Omega$, $R_{g2} = 18\ \Omega$, $R_{d1} = 100\ \Omega$, $R_{d2} = 56\ \Omega$, $R_{b1} = 470\ \Omega$, $R_{b2} = 180\ \Omega$, $R_i = 560\ \Omega$, $V_{b1} = -0.3$ V, $V_{b2} = -0.3$ V, $V_{d1} = 1.9$ V, and $V_{d2} = 1.0$ V).

As shown in Fig. 7(c), the output- and input-impedance calculated by equation (5)–(6) are located in the matched zone (i.e., $|S_{11}|$ and $|S_{22}| < -10$ dB) within a wide frequency range by utilizing the optimized resistors $R_{g1}$ and $R_{d2}$. Besides, the source resistors (i.e., $R_{b1}$ and $R_{b2}$) are used for proper transistor biasing and improving the stability, while the dc-block capacitors (i.e., $C_1$ and $C_4$) are optimized to reduce the insertion loss. Based on the aforementioned mechanisms, the GaAs FET ATF-34143 from Avago, high $Q$ capacitors, resistors, and RF inductors from Murata are utilized to implement the input and output absorptive networks. As shown in Fig. 8(a) and (b), the reflection coefficients (i.e., $S_{11}$, $S_{22}$, and $S_{33}$) of the proposed FPD are significantly reduced without suffering from the passband degeneration by introducing the absorptive networks. Meanwhile, the proposed absorptive networks improve the stopband performance. The isolation $S_{23}$ is increased due to the directional transformer function of the proposed absorptive networks.

## III. Fabrication and Measurement

Based on the principles mentioned above, a FPD operating at 2.10 GHz is fabricated, as shown in Fig. 9. The proposed FPD consumes 6.7 mW (i.e., 2.3 mW of the input absorptive network and 4.4 mW of the output absorptive networks) from the dc supply. The measurement is performed using the Agilent 5230A network analyzer over the frequency range from 0.1 to 20 GHz. The measured minimal insertion loss is 1.2 dB in passband (excluding 3 dB division loss) with in-band isolation higher than 20 dB. Meanwhile, the reflectionless ranges with return loss lower than −10 dB are extended to 10 GHz at the input port (i.e., port 1) and 13 GHz at the output ports (i.e., port 2 and port 3). Besides, the measurement shows an ultra-wide upper stopband up to 20 GHz ($9.5f_0$) with a rejection level greater than 42 dB. The fabricated FPD exhibits a compact circuit size of 27.3 mm × 29.1 mm (i.e., 0.36 $\lambda_g$ × 0.38 $\lambda_g$, where the $\lambda_g$ is the microstrip guided wavelength at 2.10 GHz). The comparison with state-of-the-arts in Table I reveals that the proposed FPD shows advantages of wide reflectionless range, good stopband performance, and high isolation.

## IV. Conclusion

This brief presents a compact FPD using novel trigonometric SIDGS cell and CG based absorptive networks. The SIDGS cells can not only provide a low-loss bandpass response but also extend the stopband to 20 GHz. Meanwhile, the proposed absorptive networks introduce a three-port wideband reflectionless operation in the FPD. Besides, high isolation is achieved by the optimized isolation resistor and the directional transfer function of reflectionless networks. Therefore, the proposed filtering power divider is attractive for practical applications with nonlinear devices.

## References


[1] B. Lee, S. Nam, and J. Lee, "Optimization-free design equations for narrowband equal-division filtering power divider with pre-specified filtering response and wideband isolation," *IEEE Trans. Circuits Syst. I, Reg. Papers*, vol. 66, no. 7, pp. 2496–2507, Jul. 2019.

[2] Q. Zhang, G. Zhang, Z. Liu, W. Chen, and W. Tang, "Dual-band filtering power divider based on a single circular patch resonator with improved bandwidths and good isolation," *IEEE Trans. Circuits Syst. II, Exp. Briefs*, vol. 68, no. 11, pp. 3411–3415, Nov. 2021.

[3] Y. Zhu, J. Wang, J. Hong, J.-X. Chen, and W. Wu, "Two- and three-way filtering power divider with harmonic suppression using triangle patch resonator," *IEEE Trans. Circuits Syst. I, Reg. Papers*, vol. 68, no. 12, pp. 5007–5017, Dec. 2021.

[4] L. Fan, H. Qian, B. Yang, G. Wang, and X. Luo, "Filtering power divider with wide stopband using open-stub loaded coupled-line and hybrid microstrip T-stub/DGS cell," in *Proc. IEEE MTT-S Int. Microw. Symp. Dig.*, Jun. 2018, pp. 1–4.

[5] C. Han, D. Tang, Z. Deng, H. J. Qian, and X. Luo, "Filtering power divider with ultrawide stopband and wideband low radiation loss using substrate integrated defected ground structure," *IEEE Microw. Wireless Compon. Lett.*, vol. 31, no. 2, pp. 113–116, Feb. 2021.

[6] A. Sajadi, A. Sheikhi, and A. Abdipour, "Analysis, simulation, and implementation of dual-band filtering power divider based on terminated coupled lines," *IEEE Trans. Circuits Syst. II, Exp. Briefs*, vol. 67, no. 11, pp. 2487–2491, Nov. 2020.

[7] G. Zhang, Y. Liu, E. Wang, and J. Yang, "Multilayer packaging SIW three-way filtering power divider with adjustable power division," *IEEE Trans. Circuits Syst. II, Exp. Briefs*, vol. 67, no. 12, pp. 3003–3007, Dec. 2020.

[8] N. Y. Brooklyn, "Reflectionless filters improve linearity and dynamic range," *Microw. J.*, vol. 58, no. 8, pp. 42–50, 2015.

[9] H.-S. Yang, "A pulse-modulated RF power amplifier system with output direct absorptive band-pass filter connection," in *Proc. IEEE MTT-S Int. Microw. Symp. Dig.*, Jun. 2021, pp. 632–634.

[10] M. A. Morgan, *Reflectionless Filters*, Norwood, MA, USA: Artech House, 2017.

[11] M. A. Morgan and T. A. Boyd, "Theoretical and experimental study of a new class of reflectionless filter," *IEEE Trans. Microw. Theory Techn.*, vol. 59, no. 5, pp. 1214–1221, May 2011.

[12] M. A. Morgan and T. A. Boyd, "Reflectionless filter structures," *IEEE Trans. Microw. Theory Techn.*, vol. 63, no. 4, pp. 1263–1271, Apr. 2015.

[13] M. A. Morgan, W. M. Groves, and T. A. Boyd, "Reflectionless filter topologies supporting arbitrary low-pass ladder prototypes," *IEEE Trans. Circuits Syst. I, Reg. Papers*, vol. 66, no. 2, pp. 594–604, Feb. 2019.

[14] A. Guilabert, M. A. Morgan, and T. A. Boyd, "Reflectionless filters for generalized elliptic transmission functions," *IEEE Trans. Circuits Syst. I, Reg. Papers*, vol. 66, no. 12, pp. 4606–4618, Dec. 2019.

[15] D. Psychogiou and R. Gómez-García, "Reflectionless adaptive RF filters: Bandpass, bandstop, and cascade designs," *IEEE Trans. Microw. Theory Techn.*, vol. 65, no. 11, pp. 4593–4605, Nov. 2017.

[16] R. Gómez-García, J.-M. Muñoz-Ferreras, and D. Psychogiou, "Symmetrical quasi-reflectionless BSFs," *IEEE Microw. Wireless Compon. Lett.*, vol. 28, no. 4, pp. 302–304, Apr. 2018.

[17] C. Liu, Z. Deng, X. Liu, and X. Luo, "A wideband bandpass filter with broad stopband and ultra-wide reflectionless range for 5G applications," in *Proc. IEEE MTT-S Int. Microw. Symp. Dig.*, Jun. 2019, pp. 834–837.

[18] R. Gómez-García, J.-M. Muñoz-Ferreras, and D. Psychogiou, "Split-type input-reflectionless multiband filters," *IEEE Microw. Wireless Compon. Lett.*, vol. 28, no. 11, pp. 981–983, Nov. 2018.

[19] W. Yu, Y. Rao, H. J. Qian, and X. Luo, "Reflectionless filtering 90° coupler using stacked cross coupled-line and loaded cross-stub," *IEEE Microw. Wireless Compon. Lett.*, vol. 30, no. 5, pp. 481–484, May 2020.

[20] M. Fan, K. Song, L. Yang, and R. Gómez-García, "Frequency-reconfigurable input-reflectionless bandpass filter and filtering power divider with constant absolute bandwidth," *IEEE Trans. Circuits Syst. II, Exp. Briefs*, vol. 68, no. 7, pp. 2424–2428, Jul. 2021.

[21] Z. Cao, X. Bi, and Q. Xu, "Tunable reflectionless filter with independently controllable dual passbands and absorbed harmonic signals," *IEEE Trans. Circuits Syst. II, Exp. Briefs*, vol. 68, no. 11, pp. 3416–3420, Nov. 2021.

[22] D. Tang, C. Han, Z. Deng, H. J. Qian, and X. Luo, "Substrate-integrated defected ground structure for single- and dual-band bandpass filters with wide stopband and low radiation loss," *IEEE Trans. Microw. Theory Techn.*, vol. 69, no. 1, pp. 659–670, Jan. 2021.

[23] J. Zhou, Y. Rao, D. Yang, H. J. Qian, and X. Luo, "Compact wideband BPF with wide stopband using substrate integrated defected ground structure," *IEEE Microw. Wireless Compon. Lett.*, vol. 31, no. 4, pp. 353–356, Apr. 2021.

[24] X. Luo, J.-C. Ma, and E.-P. Li, "Wideband bandpass filter with wide stopband using loaded BCMC stub and short-stub," *IEEE Microw. Wireless Compon. Lett.*, vol. 21, no. 7, pp. 353–355, Jul. 2011.

[25] D. Tang and X. Luo, "Compact filtering balun with wide stopband and low radiation loss using hybrid microstrip and substrate-integrated defected ground structure," *IEEE Microw. Wireless Compon. Lett.*, vol. 31, no. 6, pp. 549–552, Jun. 2021.

[26] B. Lee, S. Nam, and J. Lee, "Filtering power divider with reflectionless response and wide isolation at output ports," *IEEE Trans. Microw. Theory Techn.*, vol. 67, no. 7, pp. 2684–2692, Jul. 2019.

[27] R. Gómez-García, J.-M. Muñoz-Ferreras, and D. Psychogiou, "RF reflectionless filtering power dividers," *IEEE Trans Circuits Syst.II, Exp. Briefs*, vol. 66, no. 6, pp. 933–937, Jun. 2019.

[28] B. Lee, J. Lee, G. Lee, and J. Lee, "All-port-reflectionless narrowband filtering power divider topology with generic equations," *IEEE Trans. Circuits Syst. I, Reg. Papers*, vol. 69, no. 4, pp. 1417–1426, Apr. 2022.